

Experimental investigations on energy deposition and morphology of exploding aluminum wires in argon gas

Cite as: J. Appl. Phys. **125**, 103301 (2019); <https://doi.org/10.1063/1.5078811>

Submitted: 29 October 2018 . Accepted: 25 February 2019 . Published Online: 12 March 2019

Haoyu Liu , Junping Zhao, Zhicheng Wu , Lisong Zhang, and Qiaogen Zhang



View Online



Export Citation



CrossMark

ARTICLES YOU MAY BE INTERESTED IN

Quantitative analysis of gradient effective refractive index in silicon nanowires for broadband light trapping and anti-reflective properties

Journal of Applied Physics **125**, 103102 (2019); <https://doi.org/10.1063/1.5083902>

Optically reversible deformation of azobenzene particles prepared by a colloidal method

Journal of Applied Physics **125**, 103104 (2019); <https://doi.org/10.1063/1.5086954>

XFEM analysis of the fracture behavior of bulk superconductor in high magnetic field

Journal of Applied Physics **125**, 103901 (2019); <https://doi.org/10.1063/1.5063893>



Contact Hiden Analytical for further details:
W www.HidenAnalytical.com
E info@hiden.co.uk

CLICK TO VIEW our product catalogue

Instruments for Advanced Science



Gas Analysis

- dynamic measurement of reaction gas streams
- catalysis and thermal analysis
- molecular beam studies
- dissolved species probes
- fermentation, environmental and ecological studies



Surface Science

- UHV TPD
- SIMS
- end point detection in ion beam etch
- elemental imaging - surface mapping



Plasma Diagnostics

- plasma source characterization
- etch and deposition process reaction kinetic studies
- analysis of neutral and radical species



Vacuum Analysis

- partial pressure measurement and control of process gases
- reactive sputter process control
- vacuum diagnostics
- vacuum coating process monitoring

Experimental investigations on energy deposition and morphology of exploding aluminum wires in argon gas

Cite as: J. Appl. Phys. 125, 103301 (2019); doi: 10.1063/1.5078811

Submitted: 29 October 2018 · Accepted: 25 February 2019 ·

Published Online: 12 March 2019



View Online



Export Citation



CrossMark

Haoyu Liu, Junping Zhao,^{a)} Zhicheng Wu, Lisong Zhang, and Qiaogen Zhang

AFFILIATIONS

State Key Laboratory of Electrical Insulation and Power Equipment, Xi'an Jiaotong University, Xi'an 710049, China

^{a)}Author to whom correspondence should be addressed: junping_zhao@mail.xjtu.edu.cn

ABSTRACT

Experiments demonstrate a strong dependence of the energy deposition and morphology of exploding Al wires in argon gas on ambient pressures, charging voltage, and wire sizes. The specific energy deposition, before voltage collapse, increases with increasing ambient pressures and applied voltage but decreases with increasing wire sizes. The observation of the spatiotemporal distribution of exploding wires indicates that increased energy deposition suppresses the axial inhomogeneity, especially for large-sized wires, and improves the expansion velocity of the metal core. The expansion velocity of the wire core (100 μm in diameter, 2 cm in length) varies from ~0.49 km/s to ~2.3 km/s when the specific energy deposition increases from 1.95 eV/atom to 3.01 eV/atom. Decreased surrounding pressures also improve the expansion velocity. Furthermore, the analysis of photographs and emission spectrums demonstrates that the surrounding gases promote the formation of coronal plasmas when the pressure is no more than 50 kPa.

Published under license by AIP Publishing. <https://doi.org/10.1063/1.5078811>

I. INTRODUCTION

Electrical explosion of wires (EEW) is of great interest for basic research and numerous applications, such as wire-array Z-pinch,^{1,2} soft X-rays,³ shockwave generation,⁴ and nanoparticle preparation.^{5–7} In the effect of pulsed current, a metal wire immersed in gases is heated rapidly and goes through severe phase transition attributed to Joule energy deposition. The expanding metallic vapor is quickly cooled by collisions with surrounding gases, forming nanoparticles ultimately. For its unique advantages, such as high energy conversion efficiency, controllable size distribution, and high purity of products, EEW is a promising method for massive production of nanoparticles.

For nanoparticle preparation, most previous research studies focused on the size distribution and morphology of nanoparticles versus experimental conditions, including circuit parameters (i.e., applied voltage and current rates), ambient environment (i.e., gas species and pressures), and wire properties (i.e., materials, lengths, and diameters).^{7–9} Al₂O₃, Al, and Cu powders were synthesized by exploding wires with different wire diameters in Ref. 7. The results indicated that decreased wire diameter results in larger specific surface and smaller median diameter of nanopowders. In Ref. 8,

TiO₂ nanosized powders were synthesized by exploding Ti wires in 10–100 kPa O₂ with the relative energy (ratio of the charged energy to the vaporization energy of wires) of 4.3–51.9. The median diameter of nanoparticles decreased with increasing relative energy and decreasing ambient pressures. The density of plasma/vapor was considered as a critical influence factor on the size distribution of nanoparticles. In Ref. 9, copper and copper oxide nanopowders were synthesized with copper wires exploding in 0.05–1 bar air. It was found that the particle size distribution follows the log-normal distribution and the median diameter decreases from 31.3 nm to 23.6 nm with the pressure decreasing from 1 bar to 0.05 bar.

Although a lot of work has been done, only limited efforts have been made to study the effect of experimental parameters on the energy deposition and morphology of exploding wires in gases.^{10–12} Numerous research studies have studied energy deposition and spatiotemporal evolution of exploding thin wires (diameters no more than 30 μm) in the effect of nanosecond pulses in vacuum.^{13–17} However, for nanoparticle application, EEWs are generally driven by microsecond pulses and carried out in inert gases with large-sized wires (diameters and lengths no less than 100 μm and 2 cm, respectively). Unfortunately, the behavior of

EEW in vacuum is different from that in atmosphere. In short, characteristics of EEW in gases, especially energy deposition in the wire core and spatiotemporal distribution of exploding wires, have not been illustrated clearly until now. No doubt, such investigations are very helpful for understanding the processes and mechanisms of EEW and will serve as a reference for parameter optimization in nanoparticle application.

In this paper, a set of experimental platforms, composed of both electrical and optical diagnostic systems, is presented in Sec. II. In Sec. III, explosion processes of EEW in gases are illustrated in detail. The effect of experimental parameters on explosion processes and specific energy deposition is analyzed through electrical measurement results. Furthermore, a method of the thermodynamical (ThD) calculation is used to analyze the skin effect.¹⁸ In Sec. IV, a multi-frame camera and a laser probe are used to observe the spatiotemporal distribution of exploding wires, including luminous plasmas and high-density cores. A streak camera is also adopted to observe continuous expansion trajectories of exploding wires. In addition, discharge processes are further studied by emission spectral analysis. A summary of experimental results and conclusions is presented in Sec. V.

II. EXPERIMENTAL SETUP AND DESCRIPTION

The schematic diagram of the experimental setup is shown in Fig. 1. A group of capacitors (3 μ F in total) were charged in parallel by a high-voltage direct current (HVDC) power supply (positive, 0–50 kV) and discharged to the wire load through a trigatron, which is triggered by a pulse (~10 kV) that is synchronized to the diagnostic devices with a DG535. The argon pressure in the chamber ranges from 1 kPa to 1000 kPa.

The load current and voltage were measured by a Pearson Coil 4997 (0.01 V/A, 20 MHz bandwidth) and a homemade resistive voltage divider (0.56 mV/V, 75 MHz bandwidth), respectively. All the signals were recorded by a Tektronix Oscilloscope

MDO3024 (2.5 Gs/s sampling rate, 200 MHz bandwidth). By implementing short-circuit tests, the resistance and inductance of the external circuit were tested at 80 m Ω and 1.67 μ H. The inductance of the wire load has been taken into account to reconstruct the load resistive voltage, based on the assumption that the inductance change before the breakdown could be neglected. The specific energy deposition E is the energy deposited into the wire up to the point of voltage collapse, which is calculated by

$$E = \frac{\int_0^{t_e} U_R I dt}{N}, \quad (1)$$

$$U_R = U - (L_w + L_c) \frac{dI}{dt}, \quad (2)$$

$$L_w = 2 \times 10^{-7} l \left(\ln \frac{4l}{D} - 0.75 \right). \quad (3)$$

N is the atom number of the aluminum wire and t_e is the moment of voltage collapse. U_R and U are the resistive voltage drop and the measured voltage, respectively. L_w is the inductance of the wire and L_c is the inductance of the measurement circuit (0.58 μ H). D and l are the diameter and the length of the wire load.

The diagram of the optical diagnostic system is shown in Fig. 2. Photographs of the explosion were taken by a multi-frame optical camera (PCO HSFC Pro) with a 3 ns temporal resolution and a 121.4 μ m/pixel spatial resolution. The camera lens of the streak camera focused on the middle of wires with a 2 μ s time scale. An adjustable reflecting mirror was used to change the optical paths. To protect the recording intensified charge-coupled devices (ICCDs) from hard light, a neutral density filter [optical density (OD) = 2] was placed in front of the observation window.

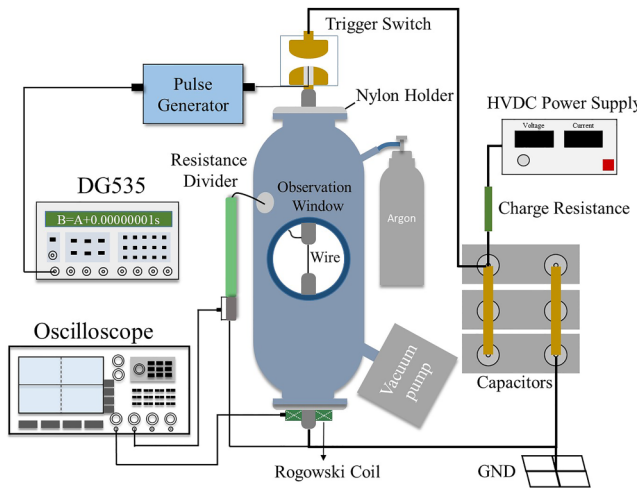


FIG. 1. Schematic diagram of the experimental setup.

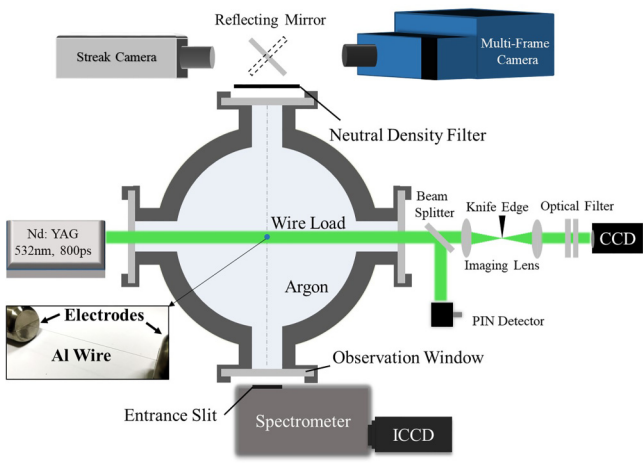


FIG. 2. Schematic diagram of the optical diagnostics system.

Based on a laser device (Nd: YAG, $\lambda = 532$ nm, $\Delta t \approx 800$ ps, $E > 20$ mJ) and an imaging system, the shadowgraphs of exploding wires were recorded by a Nikon D300. When setting a knife edge at the focus of the lens, schlieren photographs were obtained, instead of shadowgraphs. The optical filter was composed of a narrow bandpass filter ($\lambda = 532$ nm) and a neutral density filter (OD = 5). In addition, a PIN detector ET-2030 (0.47 A/W, 1.2 GHz bandwidth) was adopted to confirm the moment of the laser probe.

It should be noted that multi-frame photographs are sensitive to observe the luminous substances, including plasmas and the metal vapor. Also, laser shadowgraphs are more effective to observe the high-density cores and the shockwaves. Furthermore, schlieren imaging is a perfectly acceptable method to observe the radial distribution of exploding wires. However, both multi-frame photographs and shadowgraphs are discrete in time so that the accuracy of the results depends on the repeatability of the experiments, while the continuous expansion trajectory and light intensity of exploding wires could be obtained by streak images.

The emission light of exploding wires was collected by a spectrometer (SOL MS2001i), which is connected with the multi-frame optical camera through relay lens. The slit, the

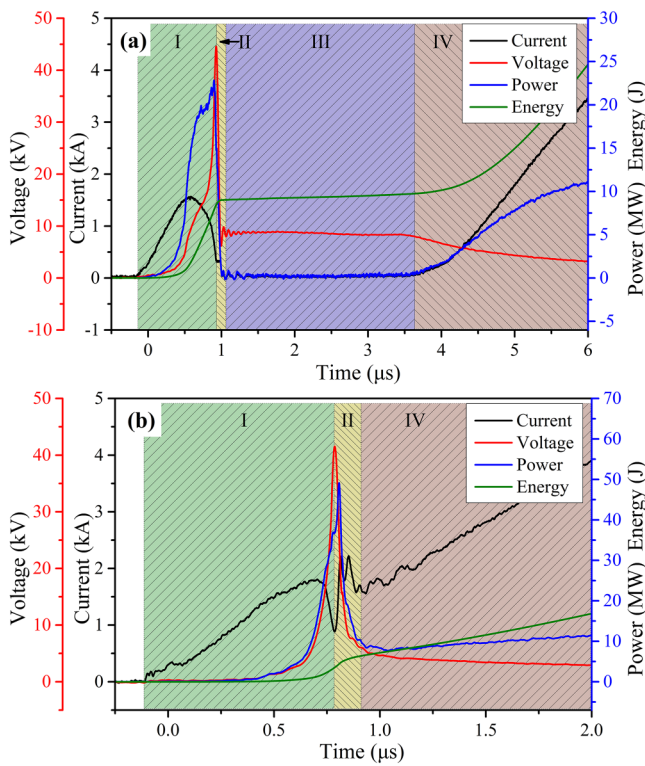


FIG. 3. Waveforms of current, voltage, power, and energy deposition when exploding Al wires (100 μm in diameter) with 10 kV charging voltage in 200 kPa argon: (a) wire length 10 cm and (b) wire length 2 cm.

wire, and the optical axial of the imaging system are orthogonal to each other so that the radiation spectra along the radius direction of the wire could be captured. The spectrometer covers a wavelength range of 420–770 nm with a 0.39 nm/pixel spectral resolution. Also, the spatial resolution along the radius direction was 9 $\mu\text{m}/\text{pixel}$, tested with a slit and a background light source. The wavelength and the efficiency of the grating and ICCDs were calibrated by a mercury lamp and a Calibrated VIS-Halogen Light source (AvaLight-HAL-CAL), respectively. To ensure the signal-to-noise ratio, the entrance slit was set 100 μm with 10 ns exposure time.

To improve production efficiency for nanoparticle application, large-sized wires are preferred and the ambient pressures generally range from dozens of kPa to hundreds of kPa. Therefore, in our research, aluminum wires (Al-99.99%, 100–400 μm in diameter, 2–10 cm in length) were exploded with 5–40 kV charging voltage in 20–1000 kPa argon.

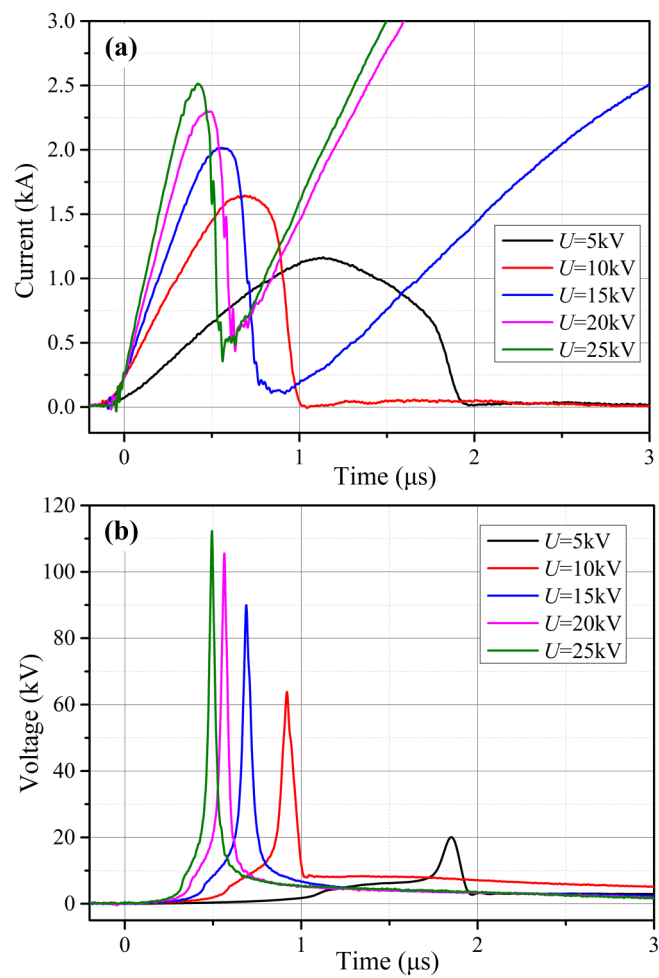


FIG. 4. Waveforms of (a) current and (b) voltage when exploding Al wires (100 μm in diameter, 6 cm in length) with 5–25 kV charging voltage in 400 kPa argon.

III. VOLT-AMPERE AND ENERGY DEPOSITION CHARACTERISTICS OF EEW

A. Wire explosion processes in gases

Electrical explosion of thin wires in vacuum is described by a sequence of three processes:¹⁹ (1) the wire is heated due to Joule energy deposition; (2) breakdown occurs in the vapor ablated from the hot wire surface, producing a hot, fast expanding corona; (3) radial switching of the current to the high-conductivity corona terminates Joule heating of the wire core. It is proposed that underwater electrical explosion is accompanied by phase transitions of the wire, namely, melting, evaporation, and plasma formation.²⁰ However, wire explosion processes in gases are somewhat different from that in vacuum and water.

In our research, EEW processes in gases are divided into four stages, namely, I: Joule heating of the wire; II: Voltage collapse; III:

Dwell time; and IV: Restrike. The waveforms of current, voltage, power, and energy deposition when exploding Al wires (100 μm in diameter, 2 cm and 10 cm in length) with 10 kV charging voltage in 200 kPa argon and stage divisions are shown in Fig. 3. Taking Fig. 3(a), for example, after the onset of the current, the wire begins as a strongly degenerate, strongly coupled (non-ideal) plasma in condensed state (i.e., solid, melting, and liquid). In stage I, rising temperature of the material results in a continuous decrease of the conductivity. Once vaporized, the wire becomes a plasma with an appreciable density of electrons, resulting from temperature delocalization and proximity delocalization. With the arrival of stage II, the gaseous-plasma wire traverses into the metal-nonmetal transition regime, which causes the conductivity to plummet, producing the current dwell (or near dwell). The dwell stage (III) features a relatively high voltage and an

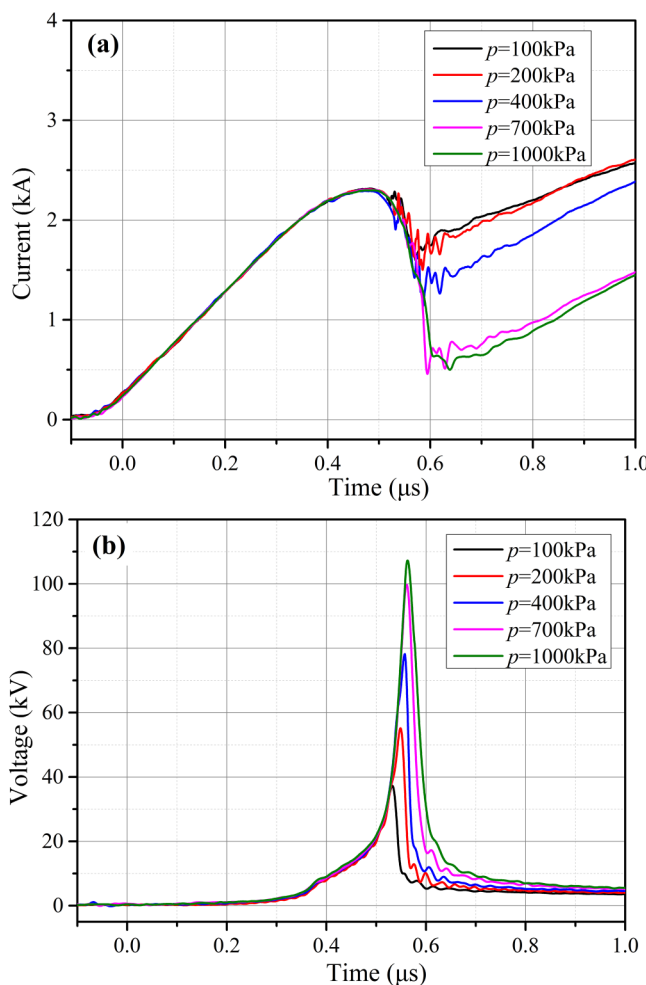


FIG. 5. Waveforms of (a) current and (b) voltage when exploding Al wires (100 μm in diameter, 4 cm in length) with 20 kV charging voltage in 100–1000 kPa argon.

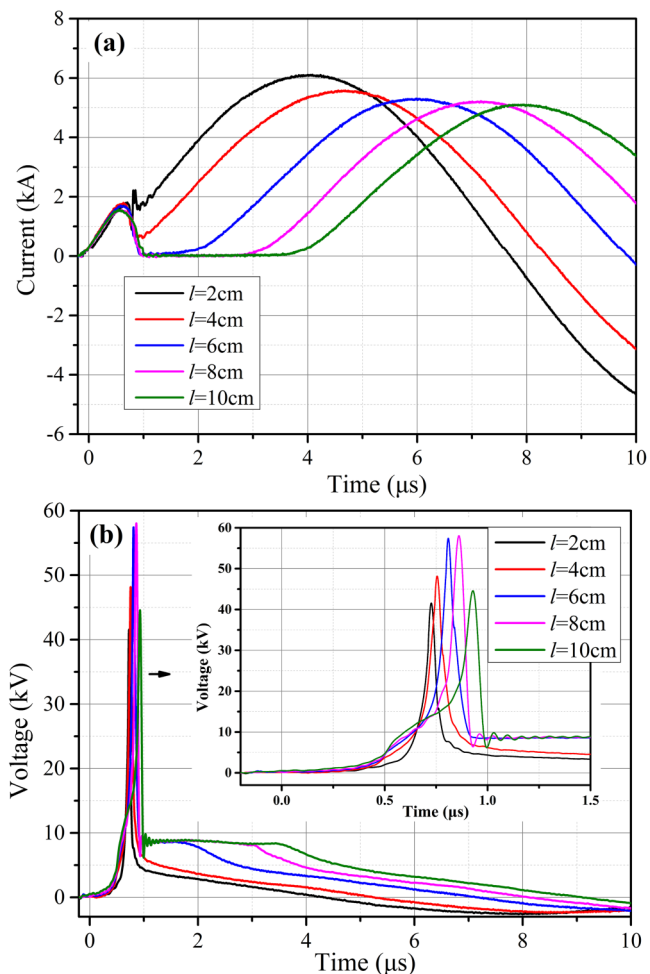


FIG. 6. Waveforms of (a) current and (b) voltage when exploding Al wires (100 μm in diameter, 2–10 cm in length) with 10 kV charging voltage in 200 kPa argon.

indiscernible current (no more than 100 A), lasting for several microseconds. In the meantime, low-conductivity of the aerosol results in interruption of the energy deposition into the wire core. However, as the wire continues to evolve hydrodynamically, even though this evolution might be slow or near stagnate in the effect of surrounding gases, it departs the non-metal regime and begins to conduct again. The restrike after dwell stage is in nature ionization of internal gas-drops cylinder because of expansion and decrease of the gas density (IV).

However in Fig. 3(b), restrike occurs immediately after voltage collapse so that there is no dwell stage. It is noteworthy that both of two explosion processes are predicted by a simple single temperature, single fluid MHD model for EEW in water and air,^{21–22} suggesting that there are no different explosion modes, but rather just different manifestations of the same physics. The only exception is when the pressure decreases to a certain extent, breakdown in the ambient gas or surface flashover along the wire might be occurring, which is discussed in Sec. IV.

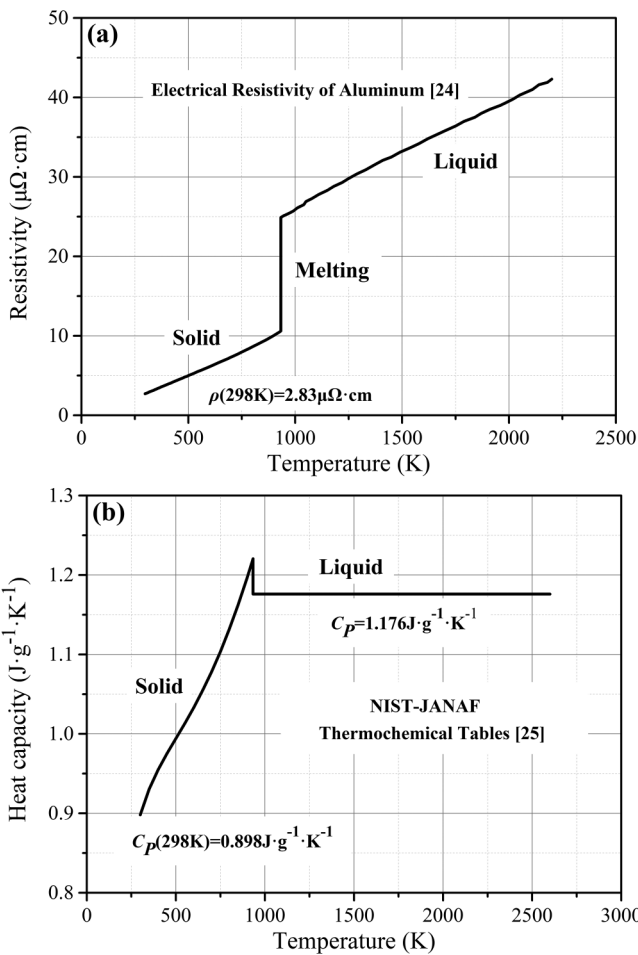


FIG. 7. Temperature dependence of (a) resistivity $\rho(T)$ and (b) heat capacity $C_p(T)$ for aluminum.

TABLE I. Aluminum constants used for the ThD calculation.

Parameter	Value	References
Low melting resistivity ρ_s	$10.6 \mu\Omega \text{ cm}$	24
High melting resistivity ρ_L	$25.0 \mu\Omega \text{ cm}$	24
Initial temperature resistivity ρ (298 K)	$2.83 \mu\Omega \text{ cm}$	24
Enthalpy of the solid stage H_s	0.67 kJ g^{-1}	25
Enthalpy of fusion H_{fusion}	0.40 kJ g^{-1}	25
Enthalpy of the liquid stage H_L	2.18 kJ g^{-1}	25
Melting temperature T_{melt}	933 K	25
Heat capacity of liquid $C_{P-\text{liquid}}$	$1.18 \text{ J g}^{-1} \text{ K}^{-1}$	25

B. Effect of experimental parameters on explosion processes

EEW in gases is complicated because several experimental parameters, including charging voltage, ambient pressures, and wire sizes (diameters and lengths), affect the explosion processes significantly.

For a specific wire, the current density through the wire is determined by the charging voltage. When exploding Al wires (100 μm in diameter, 6 cm in length) in 400 kPa argon, current and voltage waveforms with charging voltage 5–25 kV are shown in Fig. 4. It is seen from Fig. 4(a) that the current rate in early stage is approximately linear with the charging voltage. With the charging voltage increasing from 5 kV to 25 kV, duration of the resistive

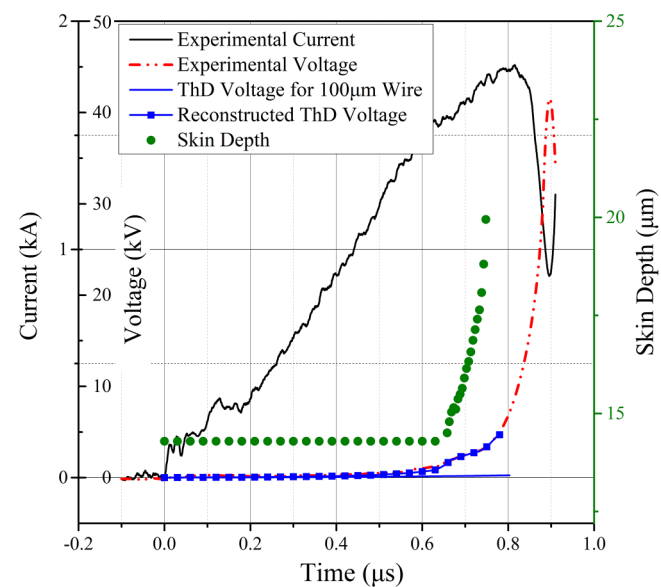


FIG. 8. Comparison of the ThD calculation with experimental results when exploding wires (100 μm in diameter, 2 cm in length) with 10 kV charging voltage in 200 kPa argon.

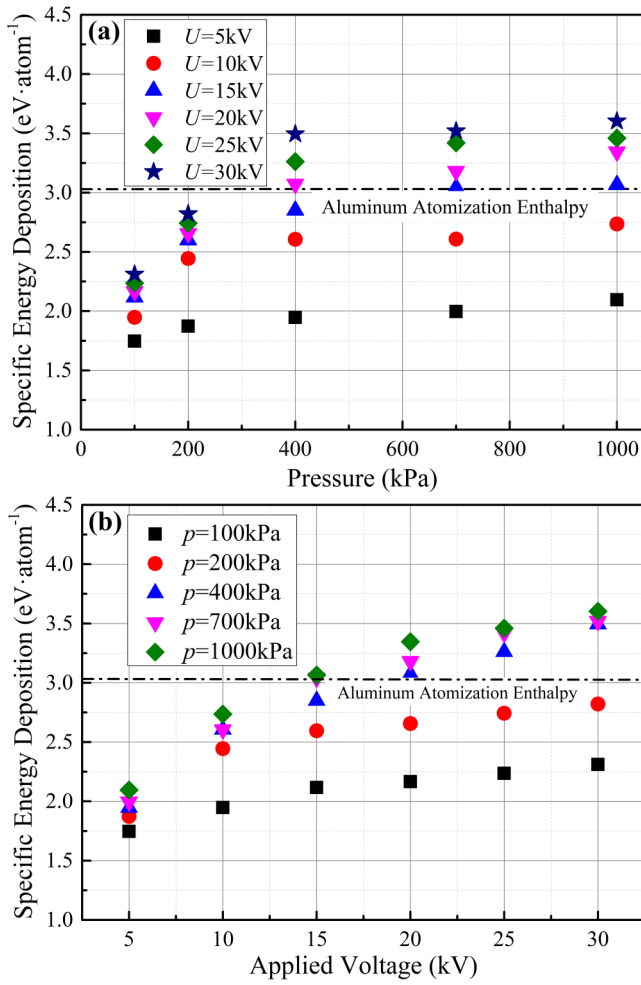


FIG. 9. Variation of the specific energy deposition of exploding Al wires (100 μm in diameter, 2 cm in length) with (a) pressure and (b) charging voltage.

stage decreases from $1.83 \mu\text{s}$ to $0.46 \mu\text{s}$ and the voltage peak increases from 20.3kV to 111.9kV , as shown in Fig. 4(b).

Surrounding gases will either promote or restrain the formation of coronal plasmas outside the wire core, depending on the ambient pressures.²³ The results in Ref. 11 demonstrated that increased gas pressure (hundreds of kPa) resulted in increased energy deposition into the wire, which was attributed to the production of a more uniform wire profile. Waveforms of current and voltage, when exploding Al wires (100 μm in diameter, 4 cm in length) with 20 kV charging voltage in 100–1000 kPa argon, are shown in Fig. 5. The results indicate that changing of the pressure hardly affects the resistive stage. With increasing pressures, expansion of exploding wires is suppressed so that restrike becomes more difficult. Prolongation of the energy deposition stage duration and increase of the voltage peak value result in more energy deposition in the wire core before voltage collapse, corresponding to the results shown in Ref. 11.

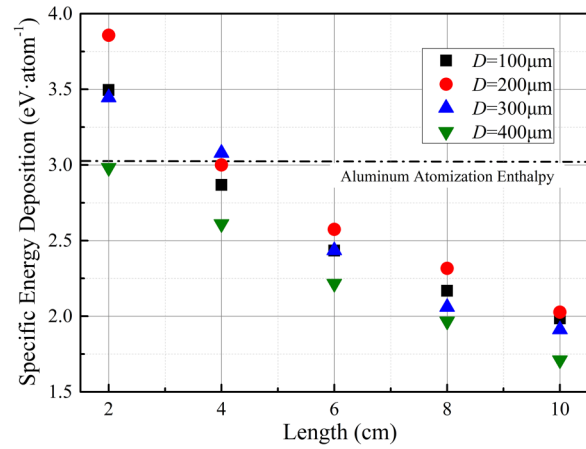


FIG. 10. Specific energy deposition of exploding Al wires (100–400 μm in diameter, 2–10 cm in length) with 30 kV charging voltage in 400 kPa argon.

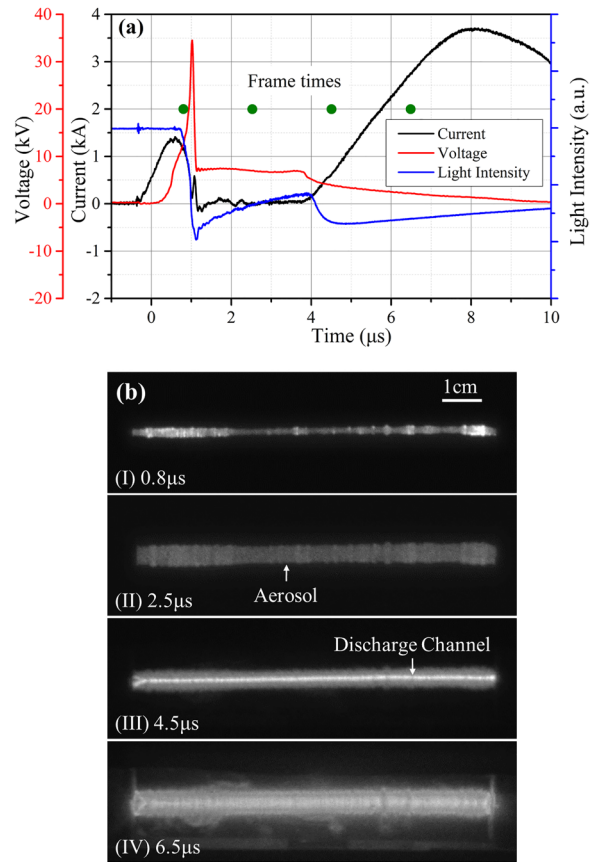


FIG. 11. (a) Waveforms of current, voltage, and light intensity and (b) multi-frame photographs of exploding Al wires (100 μm in diameter, 10 cm in length) with 10 kV charging voltage in 200 kPa at different moments: (I) 0.8 μs , (II) 2.5 μs , (III) 4.5 μs , and (IV) 6.5 μs .

Similar to increase of pressures, prolongation of wire lengths also results in an extended period of resistive stage and makes restrike more difficult. Waveforms of current and voltage, when exploding Al wires (100 μm in diameter, 2–10 cm in length) with 10 kV charging

voltage in 200 kPa argon, are shown in Fig. 6. The conditions for wire length 2 and 4 cm do not have a dwell stage. On the contrary, the dwell duration increases with length rises (0.8, 2.0, and 2.7 μs corresponding to wire length 6, 8, and 10 cm).

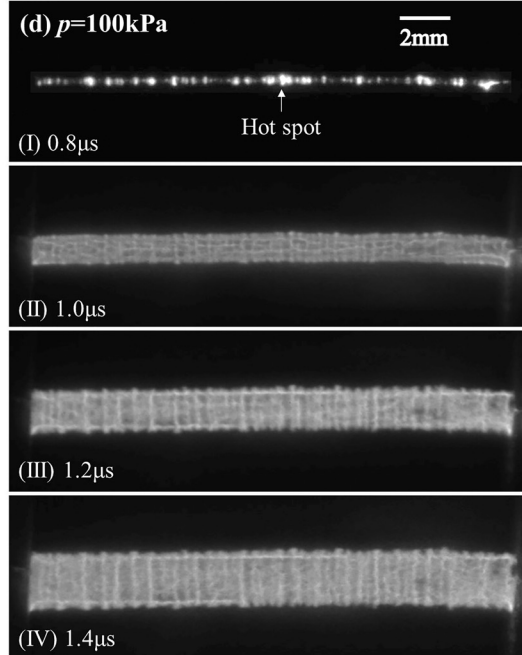
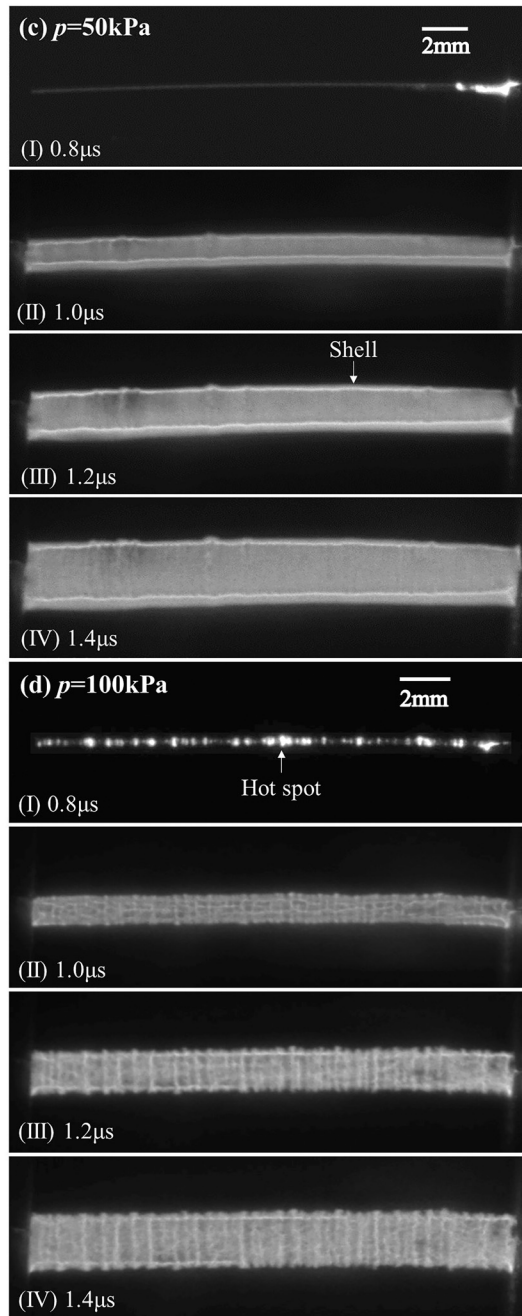
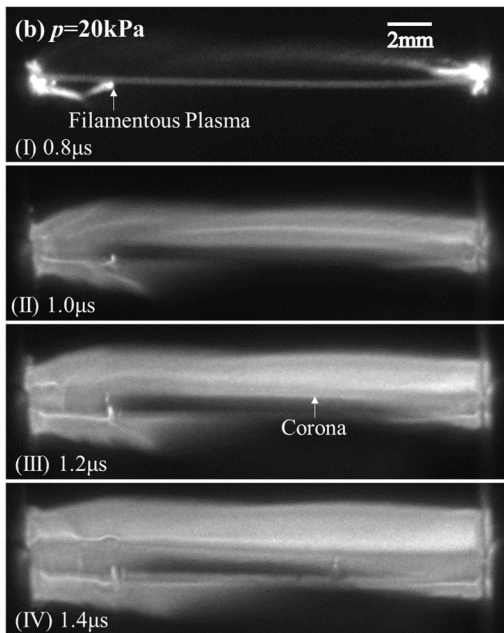
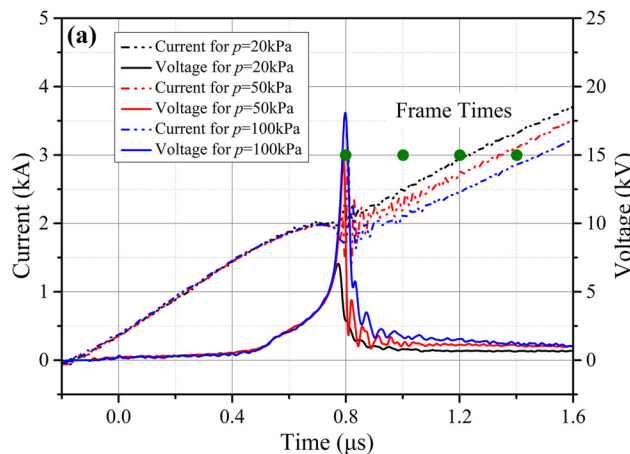


FIG. 12. (a) Current, voltage waveforms, and photographs of exploding Al wires (100 μm in diameter, 2 cm in length) with 10 kV charging voltage in (b) 20 kPa, (c) 50 kPa, and (d) 100 kPa argon.

C. Comparison of the thermodynamical calculation with experimental results

Different from thinner wires (diameter no more than 30 μm), inhomogeneity in the cross section of wires, due to the skin effect, becomes critical when exploding wires with the diameter no less than 100 μm . A simple technique for thermodynamical (ThD) calculations was used to analyze the skin effect during the energy deposition stage.¹⁸

For each time step dt , the Joule energy deposition dE and the variation of temperature dT are calculated as¹⁸

$$dE = I^2(t)\rho(T)\frac{L}{S} dt, \quad (4)$$

$$dT = \frac{dE}{mC_p(T)}, \quad (5)$$

where $\rho(T)$ and $C_p(T)$ are the temperature-dependent electrical resistivity and heat capacity at constant pressure in $\text{J g}^{-1} \text{K}^{-1}$, m is the mass of the wire in g, and T is the temperature in K.

The temperature-dependent aluminum resistivity according to Ref. 24, in $\mu\Omega \text{cm}$, is presented in Fig. 7(a). During the transition from the solid to liquid phase, the temperature is constant, and the resistivity is calculated as¹⁸

$$\rho_{\text{melt}}(E) = \rho_s + \frac{(\rho_L - \rho_s)}{H_{\text{fusion}}} (E - E_s), \quad (6)$$

where ρ_s and ρ_L are the low (solid) and high (liquid) resistivity for the melt transition and H_{fusion} is the enthalpy of fusion. The temperature-dependent heat capacitance for aluminum according to Ref. 25, in $\text{J g}^{-1} \text{K}^{-1}$, is shown in Fig. 7(b).

The coefficient of linear thermal expansion for aluminum is $2.3 \times 10^{-5} \text{ K}^{-1}$. Heating of the 100 μm diameter Al wire from 298 K up to the melting point 933 K results in 1.46% increasing of the wire diameter and 2.86% decreasing of the density. So, we will neglect the thermal expansion of the solid aluminum up to melting. Aluminum constants that we used for the ThD-calculations are shown in Table I.

When exploding Al wires (100 μm in diameter, 2 cm in length) with 10 kV charging voltage, for example, the current is shown in Fig. 6(a). According to the ThD calculation, the wire does not melt during the first 800 ns and maximum voltage stays less than 1 kV, which is quite different from experimental results as shown in Fig. 8. This means current flows through smaller cross section and the results have demonstrated that the current carrying cross section is essentially dynamic value. We have recovered it by matching ThD voltage to the experimental voltage. The step-by-step results is also shown in Fig. 8. Before 0.6 μs , the ThD voltage for the 70 μm wire is consistent with experimental voltage. Heating of the initial skin layer results in rising of the local resistivity and rejection of the current. Therefore, the skinned current penetrates inside of the metal wire from the hot and high-resistance periphery to the cold and low-resistance center. For the wire diameter more than 100 μm , the skin effect becomes more critical and results in considerably inhomogeneous heating in the cross section of the wire.

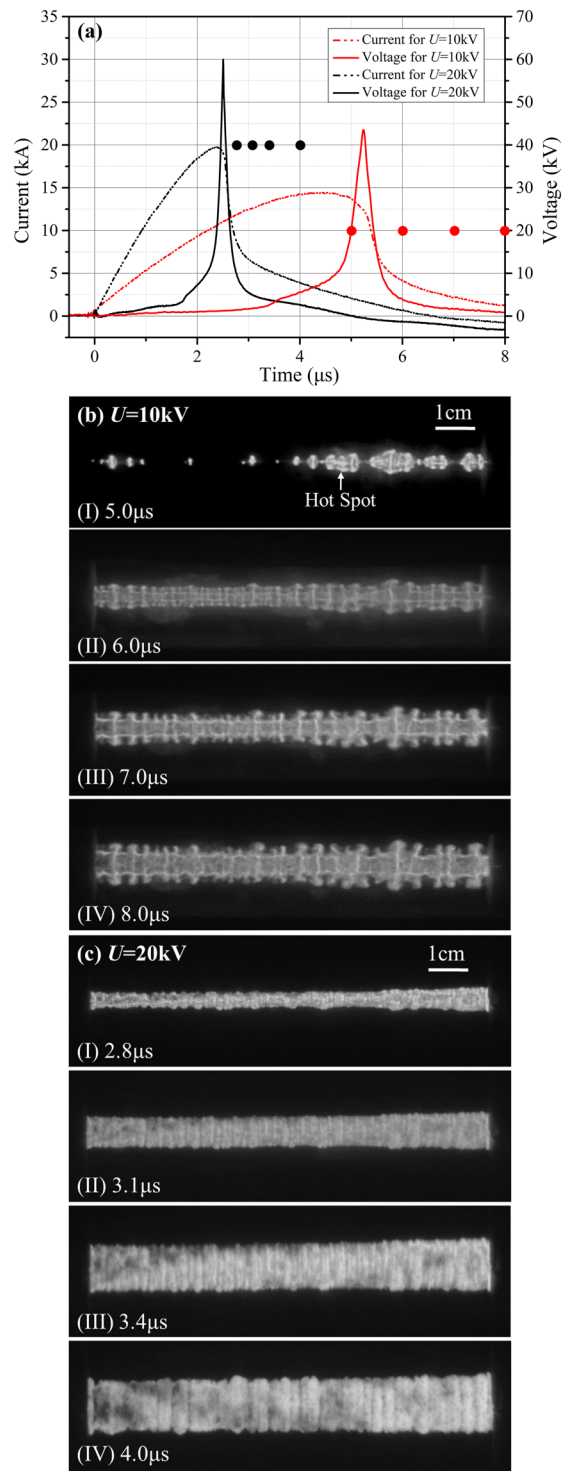


FIG. 13. (a) Current, voltage waveforms, and photographs of exploding Al wires (400 μm in diameter, 10 cm in length) with (b) 10 kV and (c) 20 kV charging voltage in 200 kPa argon.

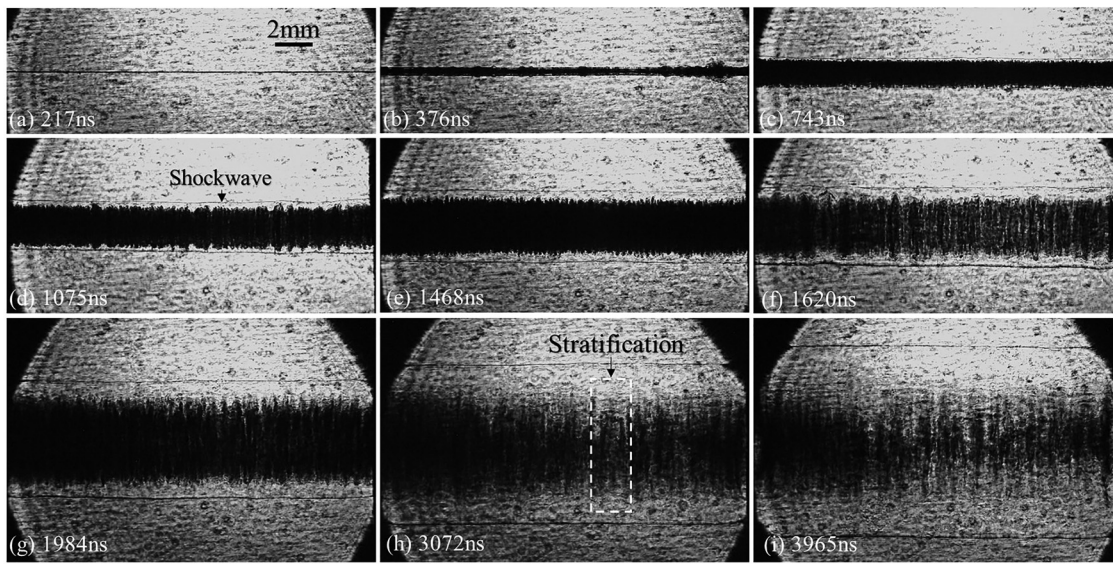


FIG. 14. Shadowgraphs of exploding Al wires (100 μm in diameter, 2 cm in length) with 15 kV charging voltage in 200 kPa argon at different moments: (a) 217 ns, (b) 376 ns, (c) 743 ns, (d) 1075 ns, (e) 1468 ns, (f) 1620 ns, (g) 1984 ns, (h) 3072 ns, and (i) 3965 ns.

D. Energy deposition characteristics of EEW

Energy deposition is an important parameter of EEW and the spatial distribution, expansion velocity, and plasma characteristics are all under its influence. The specific energy deposition of exploding Al wires (100 μm in diameter, 2 cm in length) with 5–30 kV charging voltage in 100–1000 kPa argon is shown in Fig. 9. The results demonstrated that the specific energy deposition increases as the ambient pressures and the charging voltage rise. The improvement of energy deposition by increasing pressure is significant when the pressure is no more than 400 kPa and tends to be gentle with the continuous increase of the pressure. Enhancement of charging voltage is more efficient to improve the energy deposition when the pressure is higher than 400 kPa.

In addition to ambient pressures and charging voltage, wire sizes (length and diameter) also affect the specific energy deposition, as shown in Fig. 10. The results indicate that specific energy deposition decreases with the increase of wire length. However, the effect of wire diameters on specific energy deposition is difficult to explain. When exploding thinner wires, the earlier occurrence of voltage collapse is likely to reduce energy deposition. With the increase of the wire diameter, the current density in cross section tends to be inhomogeneous due to the skin effect so that the specific energy deposition decreases. The quality reduction of the nanoparticles when exploding large-sized wires⁷ is mainly caused by the lack of specific energy deposition.

In conclusion, for a certain wire, increase of either charging voltage or ambient pressure is effective to improve the specific energy deposition before voltage collapse. For higher production efficiency, large-sized wires are priority, but the specific energy deposition tends to decrease. For nanoparticle application, only proper coordination of several parameters will meet the particular requirements.

IV. SPATIOTEMPORAL DISTRIBUTION CHARACTERISTICS OF EXPLODING WIRES

A. Multi-frame photographs

The waveforms of current, voltage, light intensity, and photographs of exploding Al wires (100 μm in diameter, 10 cm in length) with 10 kV charging voltage in 200 kPa argon are shown in Fig. 11. During the dwell stage, a low-conductivity aerosol forms, shown in

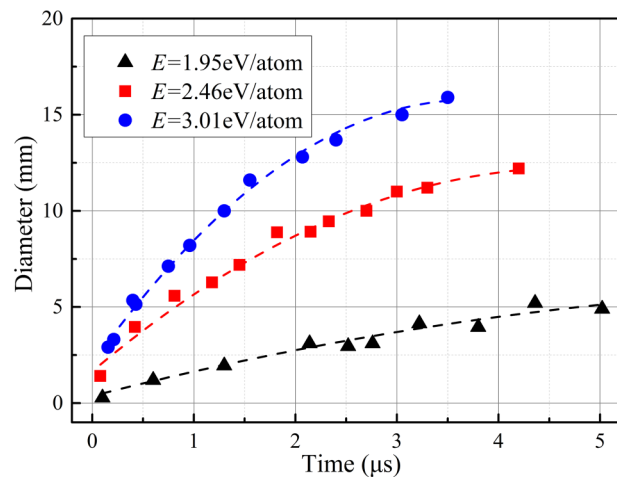


FIG. 15. Positions of the high-density region when exploding wires (100 μm in diameter, 2 cm in length) in 200 kPa argon with different specific energy deposition; dash lines are parabolic fit for the positions of metal cores.

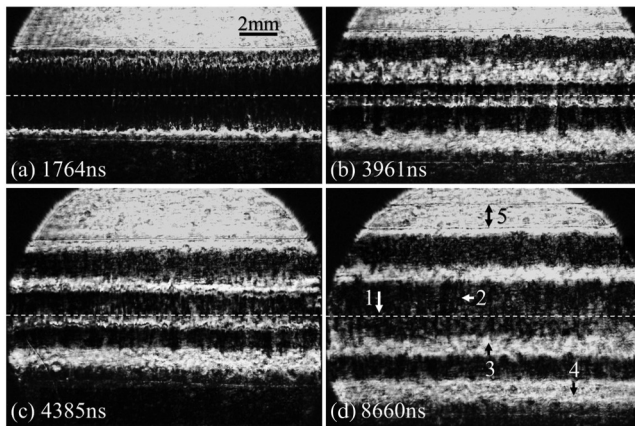


FIG. 16. Schlieren images of exploding wires ($100\text{ }\mu\text{m}$ in diameter, 2 cm in length) with 15 kV charging voltage in 1000 kPa argon at different moments: (a) 1764 ns , (b) 3961 ns , (c) 4385 ns , and (d) 8660 ns . 1, initial position of the wire; 2, high-density metal core; 3, discharge channel; 4, coronal plasma; and 5, shockwaves.

Fig. 11(b, II). With the expansion of the aerosol, a bright discharge channel with high conductivity occurs in the middle of the aerosol, resulting in shunting of the current. It is seen from **Fig. 11(b, III, IV)** that the discharge channel expands over time, which demonstrated that the current flows through the inner discharge channel instead of outer aerosol.

The waveforms of current, voltage, and photographs of exploding wires ($100\text{ }\mu\text{m}$ in diameter, 2 cm in length) with 10 kV charging voltage in 20 , 50 , and 100 kPa argon are shown in **Fig. 12**. In 20 kPa argon, the electron avalanche develops intensely in surrounding gases and forms coronal plasma outside the wire core, as shown in **Fig. 12(b)**. Formation of the high-conductivity corona terminates further energy deposition into the wire core. Next, the core is heated via plasma radiation instead of Joule energy deposition. In 100 kPa argon as shown in **Fig. 12(d)**, the electron avalanche is difficult to develop in surrounding gases so that more energy is deposited in the wire core before voltage collapse. The

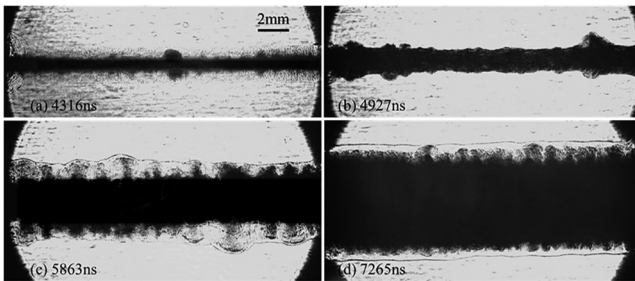


FIG. 17. Shadowgraphs of exploding wires ($400\text{ }\mu\text{m}$ in diameter, 2 cm in length) with 15 kV charging voltage in 200 kPa argon at different moments: (a) 4316 ns , (b) 4927 ns , (c) 5963 ns , and (d) 7565 ns .

significant difference, compared with the photographs in **Fig. 11(b)**, is that no evident discharge channel could be found inside the metal vapor under the circumstances. EEW in 50 kPa argon seems like a transitional circumstance. Formation of coronal plasma is suppressed to a certain extent, while the pressure is not high enough so that argon participates in the discharge process.

The spatial distribution is also significantly affected by the specific energy deposition,^{13,17} especially when exploding large-sized wires. Current, voltage waveforms, and photographs of exploding wires ($400\text{ }\mu\text{m}$ in diameter, 10 cm in length) with 10 kV and 20 kV charging voltage in 200 kPa argon are shown in **Fig. 13**. Non-inhomogeneous process of plasma generation along the wire length, due to non-equilibrium phase transition, is shown in **Fig. 13(b, I)**. When the energy deposition is insufficient for complete vaporization, classical Rayleigh-Taylor instability (R-T instability) could be observed in a boundary of expanding light fluid into heavier fluids, as shown in **Fig. 13(b, IV)**. With the charging voltage increasing to 20 kV , the spatial distribution of the exploding wire becomes much more homogeneous and expansion velocity has significant improvement. Similar electro-thermal-like features of the spatial distribution of exploding wires are also observed with ICCD images in Ref. 12.

B. Laser shadowgraphs and schlieren images

Laser shadowgraphs of exploding wires ($100\text{ }\mu\text{m}$ in diameter, 2 cm in length) with 15 kV charging voltage in 200 kPa at different moments are shown in **Fig. 14**. Before voltage collapse ($\sim 580\text{ ns}$), the diameter of the wire expands to some extent, seen in **Fig. 14(b)**. Soon, the separation of the shockwave and the metal core is

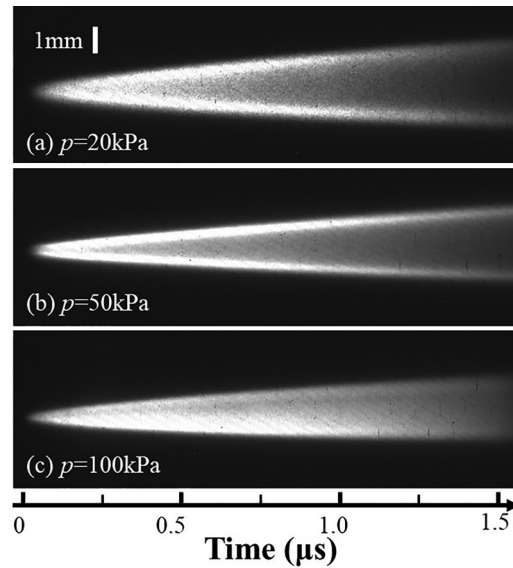


FIG. 18. Streak images of exploding Al wires ($100\text{ }\mu\text{m}$ in diameter, 2 cm in length) with 10 kV charging voltage in (a) 20 kPa , (b) 50 kPa , and (c) 100 kPa argon.

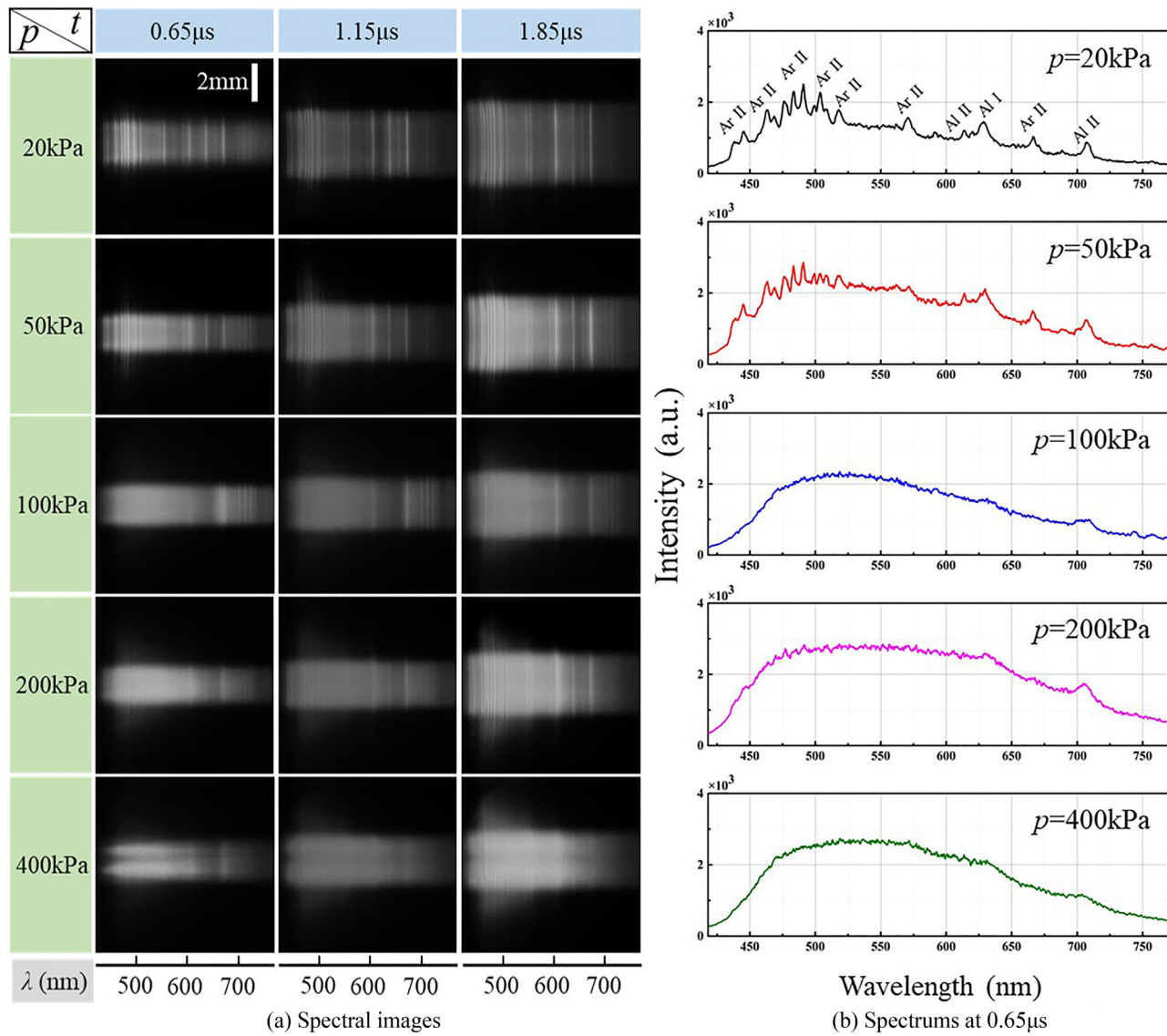


FIG. 19. Emission spectrometric results of exploding Al wires ($100\ \mu\text{m}$ in diameter, $2\ \text{cm}$ in length) with $10\ \text{kV}$ charging voltage in $20\text{--}400\ \text{kPa}$ argon at various moments: (a) spectral images and (b) spectrums at $0.65\ \mu\text{s}$.

observed in Fig. 14(d). The stratification structure shown in Figs. 14(f)–14(i), in essence alternating layers of the material with increased and decreased density, was explained by several models. The most commonly used models are the models of $m=0$ MHD instability^{26–27} and electro-thermal instability.^{28–30} In Ref. 29, for example, it was interpreted that the electrical resistivity increases with the temperature for metal wires in a condensed state, so that any small nonuniformity results in temperature perturbations that form striations perpendicular to the flow of current.

Laser shadowgraphs of exploding Al and Ag wires ($25.4\ \mu\text{m}$ in diameter, $10\ \text{mm}$ in length) in $0.015\text{--}760\ \text{Torr}$ air were presented

in Ref. 31. The results demonstrated that the expansion velocity of the metal core, at various surrounding pressures, generally agrees with Paschen's law. In addition to the ambient pressures, specific energy deposition is also found to affect significantly the expansion velocity of the metal core in surrounding gases.

The boundaries of the metal core with different specific energy deposition (1.95, 2.46, and $3.01\ \text{eV}/\text{atom}$) at different moments are presented in Fig. 15. For ease of comparison, the moment of voltage collapse is set as the original point. The trajectories correspond to parabolic paths and expansion velocities increase with the specific energy deposition (0.49, 1.65, and $2.3\ \text{km}/\text{s}$ corresponding to 1.95,

2.46, and 3.01 eV/atom, respectively). On account of the ambient gases, the expansion of metal cores is suppressed to some extent in the late stage of explosion.

The radial distribution of exploding wires (100 μm in diameter, 2 cm in length) with 15 kV charging voltage in 1000 kPa argon, with dwell stage and restrike, is clearly presented from the schlieren photographs as shown in Fig. 16. The high-density core is surrounded by low-density plasmas. The two shockwaves, generated by initial expansion and formation of internal discharge channel, respectively, are noticeable. The internal discharge channel is clearly observed and expands over time, which is coincided with the results shown in Fig. 11.

The spatial distribution of the high-density region along the axial direction is homogeneous when exploding wires with diameter no more than 100 μm . However, when exploding wires with a larger diameter (i.e., 400 μm), the inhomogeneity is significant and the R-T instability is also observed through shadowgraphs as shown in Fig. 17. Different from thinner wires, both axial and radial inhomogeneity result in the decrease of specific energy deposition, which may be the main reason for quality reduction of the nanoparticles when exploding large-sized wires.

C. Streak images

Through streak images when exploding Al wires (100 μm in diameter, 2 cm in length) with 10 kV charging voltage in 20, 50, and 100 kPa argon, continuous expansion trajectories of exploding wires and the radial distribution have been observed clearly in Fig. 18. When the ambient pressures are 20 kPa and 50 kPa, corresponding to Figs. 18(a) and 18(b), the expansion of exploding products is more likely free diffusion within 1.5 μs . Also, the surrounding shell is distinct, consistent with the photographs shown in Figs. 12(b) and 12(c). In addition, the expansion velocities decrease slightly as ambient pressure rises.

D. Emission spectrometry analysis

The spectral measurement results of exploding Al wires (100 μm in diameter, 2 cm in length) with 10 kV charging voltage in 20, 50, 100, 200, and 400 kPa argon at various moments (0.65, 1.15, and 1.85 μs) are shown in Fig. 19. The horizontal dimension and the vertical dimension represent the wavelength and the radial direction of exploding products, respectively.

When the wires are exploded in 20 kPa and 50 kPa, the characteristic peaks of Al I, Al II, and Ar II are recognizable. According to the spectrums, Al I line at 669.6 nm and Al II lines at 624.3 nm and 704.2 nm are noticeable. Also, Ar II lines at 448.2, 458.9, 460.9, 472.7, 476.5, 487.9, and 501.7 nm are also prominent. An intense broadband continuum radiation is also observed, which is most likely blackbody radiation. The emission spectrums of underwater wire explosion were analyzed through blackbody curve fitting in Ref. 32. However, the exploding wire in gases is optically thick when the material is in a condensed state. With the expansion and decrease of the density, the wire is no longer optically thick so that the spectral profile is distorted to a certain extent. With increased pressure, line radiation becomes indistinguishable and continuum spectrums become dominant. The spectral results indicate that the

argon participates in the discharge processes when the pressure is no more than 50 kPa.

V. SUMMARY

In this paper, experiments involving exploding aluminum wires (100–400 μm diameter, 2–10 cm in length) in 20–1000 kPa argon gas were carried out. Through electrical measurement and optical diagnostics, characteristics of microsecond EEW, especially energy deposition and spatiotemporal evolution, were investigated extensively.

On the basis of current and voltage waveforms, wire explosion processes in gases were analyzed by dividing into four stages and the effect of experimental parameters on explosion processes was analyzed in detail. The comparison of ThD calculations with experimental results demonstrates that the skin effect becomes critical when exploding larger wires (diameter no less than 100 μm). For a specific wire, increasing either charging voltage or ambient pressure improves the specific energy deposition in the wire core before voltage collapse, while the specific energy deposition tends to decrease with the enlargement of the wire sizes.

The morphology of exploding wires is analyzed through multi-frame photographs and laser shadowgraphs. Explosion processes with restrike feature a bright discharge channel in the middle of exploding wires after the dwell stage. Surrounding gases will either promote or restrain the formation of coronal plasmas outside the wire core so that the spatial distribution is also affected by ambient pressures. The axial inhomogeneity and Rayleigh-Taylor instability are observed when exploding large-sized wires (400 μm in diameter). It is also found that improving energy deposition is effective to suppress inhomogeneity along the axial direction. From laser shadowgraphs, evolution of the high-density region, especially the stratifications, has been observed and discussed. Diffusion of exploding wires is greatly accelerated by improving specific energy deposition.

The continuous trajectories obtained by streak images indicated that the expansion is more like free diffusion in the early stage and expansion velocities decrease with the ambient pressure rises. Furthermore, the spectral results demonstrated that when the pressure is no more than 50 kPa, gases participate in discharge processes. With the increase of the pressure, the gases tend to restrain ionization instead of promoting ionization.

ACKNOWLEDGMENTS

This work was supported by the National Natural Science Foundation of China (Grant No. 51577153). The streak images of exploding wires were taken by camera XSC110, produced by Xi'an Institute of Optics and Precision Mechanics, CAS. Thanks are given to Mr. Zhu Bingli (email: Zhubingli@opt.ac.cn) for his kind help.

REFERENCES

- ¹R. B. Spielman, C. Deeney, G. A. Chandler, M. R. Douglas, D. L. Fehl, M. K. Matzen, D. H. McDaniel, T. J. Nash, J. L. Porter, T. W. L. Sanford *et al.*, *Phys. Plasmas* **5**, 2105 (1998).
- ²D. B. Sinars, M. E. Cuneo, B. Jones, C. A. Coverdale, T. J. Nash, M. G. Mazarakis, J. L. Porter, C. Deeney, D. F. Wenger, R. G. Adams *et al.*, *Phys. Plasmas* **12**, 056303 (2005).

- ³T. A. Shelkovenko, S. A. Pikuz, D. A. Hammer, Y. S. Dimant, and A. R. Mingaleev, *Phys. Plasmas* **6**, 2840 (1999).
- ⁴A. Grinenko, S. Efimov, A. Fedotov, Y. E. Krasik, and I. Schnitzer, *J. Appl. Phys.* **100**, 113509 (2006).
- ⁵M. I. Lerner, E. A. Glazkova, A. S. Lozhkomoev, N. V. Svarovskaya, O. V. Bakina, A. V. Pervikov, and S. G. Psakhie, *Powder Technol.* **295**, 307–314 (2016).
- ⁶T. K. Sindhu, R. Sarathi, and S. R. Chakravarthy, *Nanotechnology* **19**, 025703 (2008).
- ⁷Y. A. Kotov, *J. Nanopart. Res.* **5**, 539–550 (2003).
- ⁸Y. Tokoi, T. Suzuki, T. Nakayama, H. Suematsu, F. Kaneko, and K. Niihara, *Curr. Appl. Phys.* **9**, 193–196 (2009).
- ⁹Y. S. Lee, B. Bora, S. L. Yap, and C. S. Wong, *Curr. Appl. Phys.* **12**, 199–203 (2012).
- ¹⁰Z. Mao, X. Zou, X. Wang, and W. Jiang, *Appl. Phys. Lett.* **94**, 181501 (2009).
- ¹¹J. Stephens, W. Mischke, and A. Neuber, *IEEE Trans. Plasma Sci.* **40**(10), 2517–2522 (2012).
- ¹²J. Stephens, A. Neuber, and M. Kristiansen, *Phys. Plasmas* **19**, 032702 (2012).
- ¹³G. S. Sarkisov, K. W. Struve, and D. H. McDaniel, *Phys. Plasmas* **11**(10), 4573 (2004).
- ¹⁴G. S. Sarkisov, S. E. Rosenthal, and K. W. Struve, *Phys. Rev. E* **77**, 056406 (2008).
- ¹⁵A. G. Roussikh, V. I. Oreshkin, A. Zhigalin, I. I. Beilis, and R. B. Baksht, *Phys. Plasmas* **17**, 033505 (2010).
- ¹⁶K. Wang, Z. Shi, Y. Shi, and Z. Zhao, *AIP Adv.* **7**, 095002 (2017).
- ¹⁷G. S. Sarkisov, K. W. Struve, and D. H. McDaniel, *Phys. Plasmas* **12**, 052702 (2005).
- ¹⁸G. S. Sarkisov, S. E. Rosenthal, and K. W. Struve, *Rev. Sci. Instrum.* **78**, 043505 (2007).
- ¹⁹G. S. Sarkisov, S. E. Rosenthal, K. W. Cochrane, K. W. Struve, C. Deeney, and D. H. McDaniel, *Phys. Rev. E* **71**, 046404 (2005).
- ²⁰V. T. Gurovich, A. Grinenko, Y. E. Krasik, and J. Felsteiner, *Phys. Rev. E* **69**, 036402 (2004).
- ²¹K. Chung, K. Lee, Y. S. Hwang, and D. Kim, *J. Appl. Phys.* **120**, 203301 (2016).
- ²²A. E. Barysevich and S. L. Cherka, *Phys. Plasmas* **18**, 052703 (2011).
- ²³J. Zhao, Z. Xu, W. Yan, H. Liu, and Q. Zhang, *IEEE Trans. Plasma Sci.* **45**(2), 185 (2017).
- ²⁴P. D. Desai, H. M. James, and C. Y. Ho, *J. Phys. Chem. Ref. Data* **13**(4), 1131–1172 (1984).
- ²⁵M. W. Chase, *NIST-JANAF Thermochemical Tables*, 4th ed. (J. Phys. Chem. Ref. Data Monogr. **9**, NIST Gaithersburg, MD, 1998).
- ²⁶K. B. Abramova, N. A. Zlatin, and B. P. Peregrud, *Sov. Phys. JETP* **42**(6), 1019–1026 (1975).
- ²⁷J. P. Chittenden, S. V. Lebedev, J. Ruiz-Camacho, F. N. Beg, S. N. Bland, C. A. Jennings, A. R. Bell, M. G. Haines, S. A. Pikuz, T. A. Shekovenko, and D. A. Hammer, *Phys. Rev. E* **61**(4), 4370–4380 (2000).
- ²⁸V. I. Oreshkin, *Phys. Plasmas* **15**, 092103 (2008).
- ²⁹A. G. Roussikh, V. I. Oreshkin, S. A. Chaikovsky, N. A. Labetskaya, A. V. Shishlov, I. I. Beilis, and R. B. Baksht, *Phys. Plasmas* **15**, 102706 (2008).
- ³⁰J. Wu, Y. Lu, X. Li, D. Zhang, and A. Qiu, *Phys. Plasmas* **24**, 112701 (2017).
- ³¹G. S. Sarkisov, J. Caplinger, F. Parada, and V. I. Sotnikov, *J. Appl. Phys.* **120**, 123303 (2016).
- ³²A. Grinenko, Y. E. Krasik, S. Efimov, A. Fedotov, V. T. Gurovich, and V. I. Oreshkin, *Phys. Plasmas* **13**, 042701 (2006).